Commun Nonlinear Sci Numer Simulat 62 (2018) 61–77

Contents lists available at ScienceDirect

Commun Nonlinear Sci Numer Simulat

journal homepage: www.elsevier.com/locate/cnsns

Research paper

Modeling and simulation of the hexagonal pattern formation of honeycombs by the immersed boundary method

Darae Jeong, Yongho Choi, Junseok Kim*

Department of Mathematics, Korea University, Seoul 02841, Republic of Korea

ARTICLE INFO

Article history:
Received 19 September 2017
Revised 8 January 2018
Accepted 17 February 2018
Available online 19 February 2018

Keywords:
Honeycomb
Hexagonal pattern
Immersed boundary method

ABSTRACT

We present a simple mathematical model and numerical simulations of the hexagonal pattern formation of a honeycomb using the immersed boundary method. In our model, we assume that the cells have a circular shape at their inception and that there is a force acting upon the entire circumference of the cell. The net force from the individual cells is a key factor in their transformation from a circular shape to a rounded hexagonal shape. Numerical experiments using the proposed mathematical model confirm the hexagonal patterns observed in honeybee colonies.

1. Introduction

Honeybee nests are organized into parallel and vertically aligned self-synthesized wax combs. Both sides of the comb consist of arrays of hexagonal cells that house the brood and store resources. In a regular hexagonal cell, the six sides adjoin at a 120° degree angle [1]. The hexagonal structure appears in several studies in various research fields, such as pattern formation [2], honeycomb network [3], cationic liposome-DNA [4], and honeycomb formation [1,5]. The honeycomb is the most studied natural cellular structure [6]. Despite this, there is an ongoing debate about how these hexagonal cells are produced. For example, according to some sources, the comb structure is a result of a thermoplastic wax reaching a liquid equilibrium [7]. However, according to other researchers, the hexagonal structure is not produced via a liquid equilibrium process [1]. It was reported that the cells in a natural honeybee comb have a circular shape at inception but quickly transform into the well-known rounded hexagonal shape, see Fig. 1. Several studies on the honeycomb structure have been carried out [5,8].

In this study, we propose a simple mathematical model and perform numerical simulations of the hexagonal pattern formation of a honeycomb using the immersed boundary method [9]. The basic mechanism of our model as follows: First, we set the cells which have a circular shape at their birth. Second, we compute forces acting upon the entire circumference of the individual cells. Third, we calculate the net force from the individual cells. Fourth, we move the cell boundaries according to the net force. We repeat these last three steps until it reaches an equilibrium state or a specified time. Computational experiments of the proposed mathematical model demonstrate the hexagonal patterns observed in honeybee colonies.

The importance and advantage of the studied model is that we can generate complex hexagonal pattern using a simple mathematical model and has applications such as patient-specific 3D-printed cast, which will be described in more detail in Section 3.10.

* Corresponding author.
E-mail address: cfdkim@korea.ac.kr (J. Kim).
URL: http://math.korea.ac.kr/~cfdkim/ (J. Kim)

https://doi.org/10.1016/j.cnsns.2018.02.024
1007-5704/

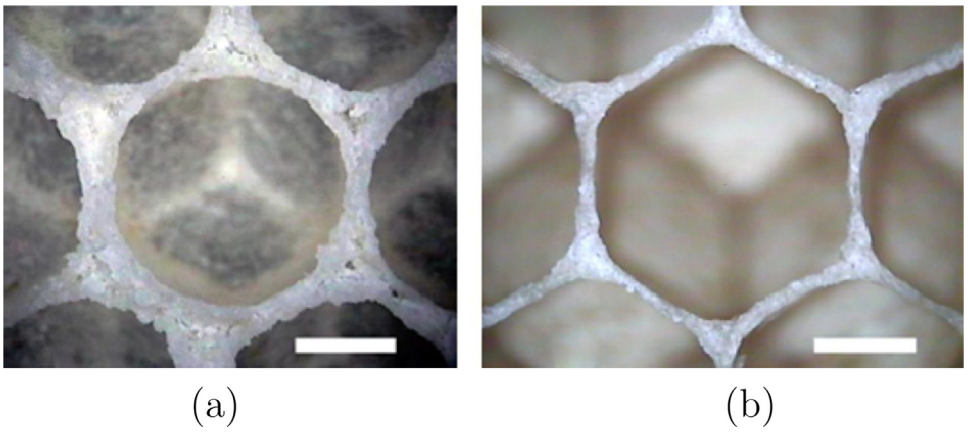

Fig. 1. Italian honeybee comb cell. (a) Inception and at (b) 2-day-old, scale bar is 2 mm. Reprinted from Karihaloo et al. [6] with permission from the Royal Society.

The novelty of the paper is to propose a mathematical model for a fundamental formation of hexagonal honeycomb structure and apply an efficient and accurate numerical method for solving the governing equation.

To the authors' knowledge this is the first attempt to model and simulate hexagonal pattern formation of the honeycomb structure in a large scale, including the interactions of cells. So far, most researches on hexagonal pattern formation focused on self-organized formation of hexagonal pattern through phase separation [10] or investigated the strength and stiffness under shear or compression [11–15].

The organization of this paper is as follows. In Section 2, we present the proposed mathematical model and numerical method for the hexagonal pattern formation. We present the simulation results in Section 3. In Section 4, conclusions are presented.

2. Mathematical model and numerical method

To model and simulate the hexagonal pattern formation of the honeycomb, we use the immersed boundary method (IBM) as a computational tool. This method was introduced by Peskin to study flow patterns around heart valves [9]. The IBM has been used by several researchers in various studies [16,17].

In the IBM, the fluid is represented on an Eulerian coordinate and the elastic structure is represented on a Lagrangian coordinate. The immersed elastic structures are typically represented as a collection of points. The velocity and pressure are defined on the Eulerian coordinate. The force exerted by the flexible structure on the fluid is considered as a source term in the momentum equation using a Dirac-delta function. Then, the Lagrangian points move with the fluid velocity interpolated through the Dirac-delta function. The governing equations are discretized by an Eulerian grid on the fluid and a Lagrangian grid on the immersed boundary. Approximations of the Dirac-delta function by a smoother function allow us to interpolate between the Eulerian and Lagrangian coordinates. Please refer to [18,19] and references therein for more details about the IBM.

Let $\mathbf{X}_k(s,t) = (\tilde{x}_k(s,t), \tilde{y}_k(s,t))$ be the immersed boundary for the kth cell at time t for $1 \le k \le N_k$, where $0 \le s \le L_k(t)$ and $L_k(t)$ is the time-dependent length of the k-th boundary. Here, N_k is the number of closed loops. Because the boundary is a closed curve, $\mathbf{X}_k(0,t) = \mathbf{X}_k(L_k(t),t)$. See Fig. 2.

We assume the cell boundaries move according to a net force on the boundaries and propose the following evolution equation:

$$\frac{\partial \mathbf{X}_k(s,t)}{\partial t} = \alpha \mathbf{F}(\mathbf{X}_k(s,t)), \tag{1}$$

where α is a proportional constant value and $\mathbf{F}$ is the net force resulting from the forces exerted outwardly by the individual cell boundaries, such as mechanical force or the heat flux caused by the honeybees [7]. Eq. (1) can be considered as a special case of the general Lagrange's equations of motion for $\mathbf{X}_k$ [20]. Lagrangian simulations have been studied in various fields [21,22].

Let a computational domain $\Omega = (0, L_x) \times (0, L_y)$ be partitioned in Cartesian geometry into a uniform mesh with mesh spacing h as shown in Fig. 2. The center of each computational cell Ω_{ij} is located at $\mathbf{x}_{ij} = (x_i, y_j) = ((i-0.5)h, (j-0.5)h)$ for $i = 1, \ldots, N_x$ and $j = 1, \ldots, N_y$. Here, N_x and N_y are the numbers of cells in the x- and y-directions, respectively. We use M Lagrangian points $\mathbf{X}^n_{k,l} = (\tilde{x}^n_{k,l}, \tilde{y}^n_{k,l})$ for $l = 1, \ldots, M$ at $t = n\Delta t$ to discretize the kth immersed boundary. Here, Δt is the temporal step size. At $\mathbf{X}^n_{k,l}$, the corresponding outward unit normal vector $\mathbf{n}^n_{k,l}$ can be calculated by using three points $\mathbf{X}^n_{k,l-1}$, $\mathbf{X}^n_{k,l}$, $\mathbf{X}^n_{k,l+1}$ with the quadratic polynomial approximations [23]

$$\tilde{x}(t) = \alpha_1 t^2 + \beta_1 t + \gamma_1 \quad \text{and} \quad \tilde{y}(t) = \alpha_2 t^2 + \beta_2 t + \gamma_2.$$

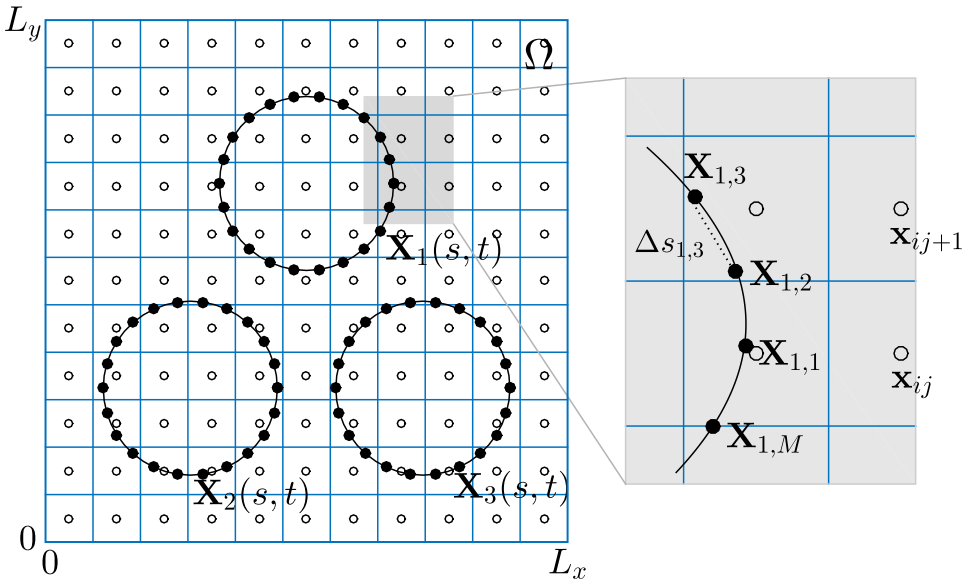

Fig. 2. Schematic illustration of computational configuration when $N_k = 3$. Here, Eulerian points $\mathbf{x}_{ij}$ and Lagrangian points $X^n_{k,l}$ $(k = 1, 2, 3)$ are denoted by open and solid circles, respectively.

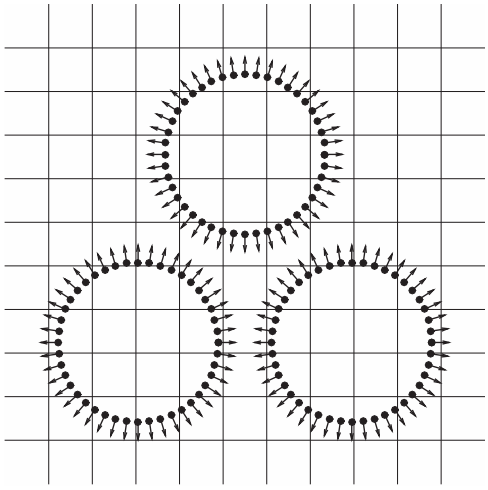

Fig. 3. Schematic illustration of normal boundary force $\mathbf{f}^n_{k,l}$ per unit length when $N_k = 3$.

For convenience, we assume that $\mathbf{X}_{k,l-1} = (\tilde{x}(0), \tilde{y}(0))$, $\mathbf{X}_{k,l} = (\tilde{x}(\Delta s_{k,l}), \tilde{y}(\Delta s_{k,l}))$, and $\mathbf{X}_{k,l+1} = \big(\tilde{x}(\Delta s_{k,l} + \Delta s_{k,l+1}), \tilde{y}(\Delta s_{k,l} + \Delta s_{k,l+1})\big)$. Here,

$$\Delta s_{k,l} = \sqrt{(\tilde{x}_{k,l} - \tilde{x}_{k,l-1})^2 + (\tilde{y}_{k,l} - \tilde{y}_{k,l-1})^2}.$$

Then, the parameters α_1, β_1, γ_1, α_2, β_2, and γ_2 can be obtained by

$$\begin{pmatrix}\alpha_1\\ \beta_1\\ \gamma_1\end{pmatrix} = \begin{pmatrix} 0 & 0 & 1\\ \Delta s^2_{k,l} & \Delta s_{k,l} & 1\\ (\Delta s_{k,l} + \Delta s_{k,l+1})^2 & \Delta s_{k,l} + \Delta s_{k,l+1} & 1\end{pmatrix}^{-1} \begin{pmatrix}\tilde{x}(0)\\ \tilde{x}\big(\Delta s_{k,l}\big)\\ \tilde{x}\big(\Delta s_{k,l} + \Delta s_{k,l+1}\big)\end{pmatrix},$$

$$\begin{pmatrix}\alpha_2\\ \beta_2\\ \gamma_2\end{pmatrix} = \begin{pmatrix} 0 & 0 & 1\\ \Delta s^2_{k,l} & \Delta s_{k,l} & 1\\ (\Delta s_{k,l} + \Delta s_{k,l+1})^2 & \Delta s_{k,l} + \Delta s_{k,l+1} & 1\end{pmatrix}^{-1} \begin{pmatrix}\tilde{y}(0)\\ \tilde{y}\big(\Delta s_{k,l}\big)\\ \tilde{y}\big(\Delta s_{k,l} + \Delta s_{k,l+1}\big)\end{pmatrix}.$$

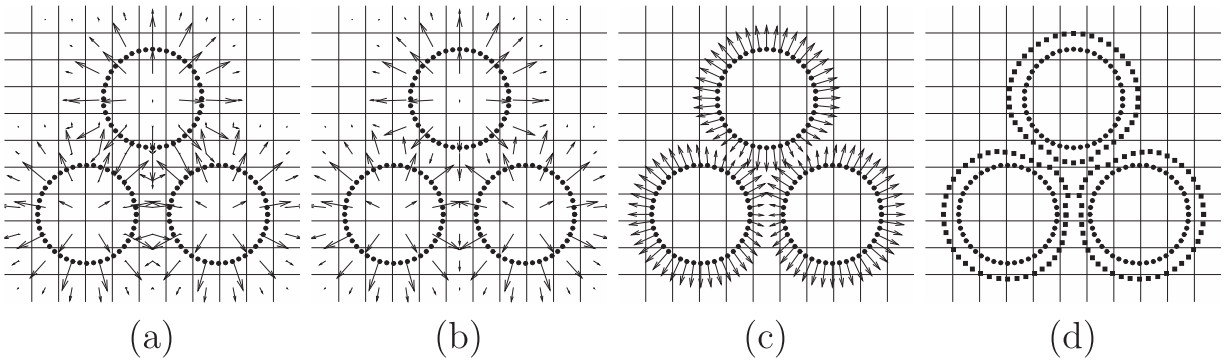

Fig. 4. Schematic illustration of the proposed model: (a) superpositioned boundary force density on Eulerian points, (b) net force on Eulerian points, (c) interpolated net force $\mathbf{F}_{ij}^n$ on Lagrangian points, and (d) updated Lagrangian points $\mathbf{X}_{k,l}^{n+1}$ (solid square) by $\mathbf{X}_{k,l}^n$ (solid circle).

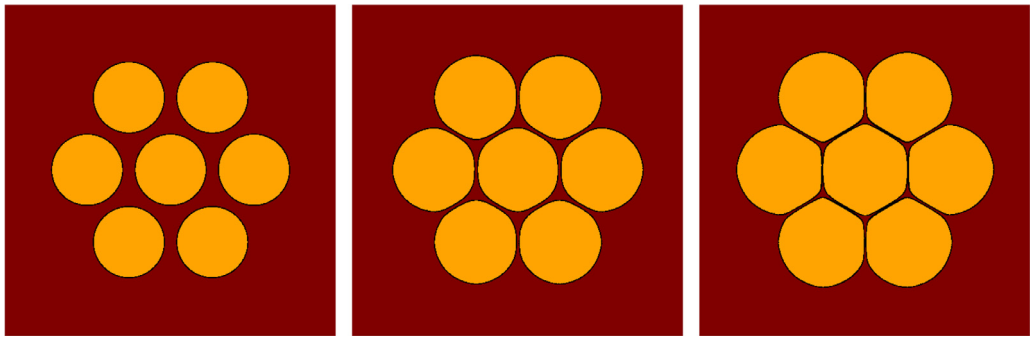

Fig. 5. Temporal evolution of initial circles by the proposed model.

Now we get the unit normal vector $\mathbf{n}_{k,l}$ as

$$\mathbf{n}_{k,l} = \left(\frac{T_y}{\sqrt{T_x^2 + T_y^2}}, \frac{-T_x}{\sqrt{T_x^2 + T_y^2}} \right),$$

where T_x and T_y are defined as

$$T_x = \frac{d\tilde{x}}{dt}\left(\Delta s_{k,l}\right) = \frac{\Delta s_{k,l}^2\left(\tilde{x}_{k,l+1} - \tilde{x}_{k,l}\right) + \Delta s_{k,l+1}^2\left(\tilde{x}_{k,l} - \tilde{x}_{k,l-1}\right)}{\Delta s_{k,l}\Delta s_{k,l+1}\left(\Delta s_{k,l} + \Delta s_{k,l+1}\right)},$$

$$T_y = \frac{d\tilde{y}}{dt}\left(\Delta s_{k,l}\right) = \frac{\Delta s_{k,l}^2\left(\tilde{y}_{k,l+1} - \tilde{y}_{k,l}\right) + \Delta s_{k,l+1}^2\left(\tilde{y}_{k,l} - \tilde{y}_{k,l-1}\right)}{\Delta s_{k,l}\Delta s_{k,l+1}\left(\Delta s_{k,l} + \Delta s_{k,l+1}\right)}.$$

Another approach for the derivation of the unit normal vector can be found in the Appendix. We define the boundary force per unit length $\mathbf{f}_{k,l}^n = \sigma \mathbf{n}_{k,l}^n$, where σ is a magnitude constant. See Fig. 3.

To compute the net force density, we first spread the boundary force over the nearby lattice points as follows:

$$\mathbf{F}_{ij}^n = \sum_{k=1}^{N_k}\sum_{l=1}^{M} \mathbf{f}_{k,l}^n \delta_h^2(\mathbf{x}_{ij} - \mathbf{X}_{k,l}^n)(\Delta s_{k,l}^n + \Delta s_{k,l+1}^n)/2, \tag{2}$$

where $\delta_h^2(x,y) = h^{-2}\phi(x/h)\phi(y/h)$ is a smoothed Dirac delta function [19] and

$$\phi(r) = \begin{cases} (3 - 2|r| + \sqrt{1 + 4|r| - 4r^2})/8 & \text{if } |r| < 1, \\ (5 - 2|r| + \sqrt{9 - 4|r| + 4(2 - |r|)^2})/8 & \text{if } 1 \le |r| \le 2, \\ 0 & \text{otherwise.} \end{cases}$$

For $k = 1, \ldots, N_k$ and $l = 1, \ldots, M$, we can move the immersed boundary points as follows.

$$\mathbf{X}_{k,l}^{n+1} = \mathbf{X}_{k,l}^n + \Delta t \sum_{i=1}^{N_x}\sum_{j=1}^{N_y} \alpha \mathbf{F}_{ij}^n \delta_h^2(\mathbf{x}_{ij} - \mathbf{X}_{k,l}^n)h^2. \tag{3}$$

This completes the one time step.

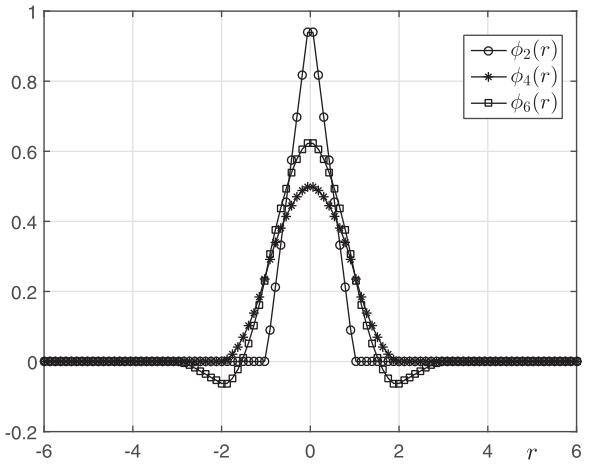

Fig. 6. Three types of Dirac delta functions.

Fig. 4 illustrates the basic mechanism of the proposed mathematical model that describes the formation of hexagonal honeycomb structure.

The formation of hexagonal honeycomb structure can be summarized in the following algorithm:

Algorithm 1 Algorithm for the formation of hexagonal honeycomb structure.

Require: N_k : total number of the cells
M: number of the immersed boundary points of the cell
r: radius of the cell
χ : control value for the target area A_{TA}
tol : tolerance for the stopping criterion
for $k = 1 : N_k$ **do**
Define the center of the cell $(c_{k,x}, c_{k,y})$.
for $l = 1 : M$ **do**
Set $\theta = 2\pi\,(l-1)/M$.
Define the Lagrangian points as

$$\mathbf{X}^0_{k,l} = (\tilde{x}^0_{k,l}, \tilde{y}^0_{k,l}) = (c_{k,x} + r\cos\theta, c_{k,y} + r\sin\theta).$$

end for
Set $\mathbf{X}^0_{k,0} = \mathbf{X}^0_{k,M}$ and $\mathbf{X}^0_{k,M+1} = \mathbf{X}^0_{k,1}$.
end for

Define the critical area as $A = \chi\pi\,(d/2)^2$, where d is the distance between the centers of two adjacent cells (see Fig. 11).
while $\|\mathbf{F}^n\|_\infty > tol$ **do**
Set $\mathbf{f}^n_{k,l} = (0,0)$ and $\mathbf{F}^n_{ij} = (0,0)$.
for $k = 1 : N_k$ **do**
Calculate area A_k of each cell as

$$A_k = \frac{1}{2}\left|\sum_{l=1}^{M}\left(\tilde{x}^n_{k,l}\tilde{y}^n_{k,l+1} - \tilde{x}^n_{k,l+1}\tilde{y}^n_{k,l}\right)\right|.$$

if $A_k < A$ **then**
Set the boundary force $\mathbf{f}^n_{k,l}$ of the kth-cell.
end if
end for
Compute the net force density $\mathbf{F}^n$ by spreading the boundary force $\mathbf{f}^n_{k,l}$ to the Cartesian grid by Eq. (2).
Move the Lagrange points by Eq. (3).
Set $n = n + 1$.
end while

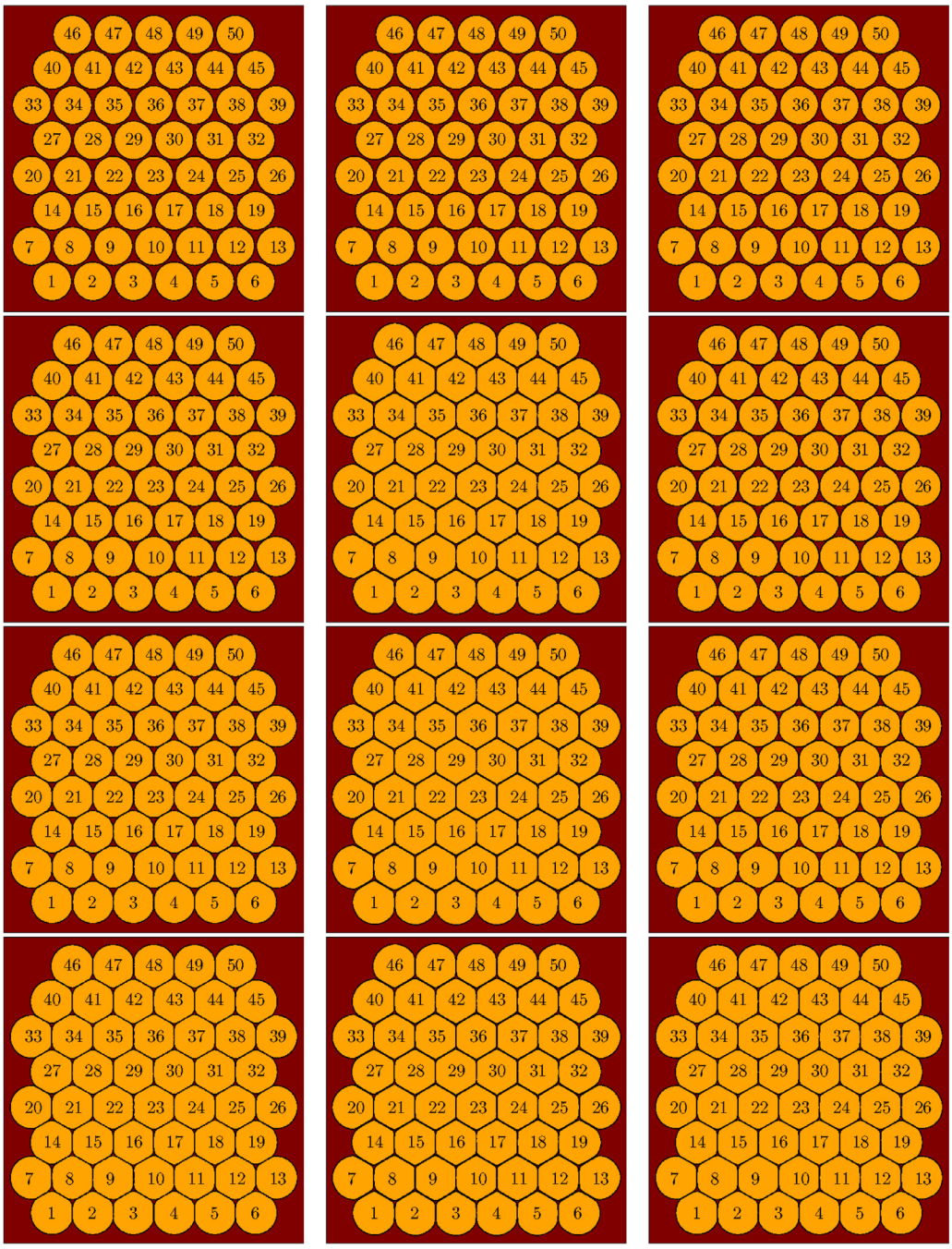

Fig. 7. Comparison study of three types of Dirac delta functions at $t = 0$ (first row), $t = 250\Delta t$ (second row), $t = 500\Delta t$ (third row), $t = 1000\Delta t$ (fourth row).

3. Simulation results

The proposed algorithm was implemented using C language on a dual 3.10GHz and 4GB Intel PC. The graphic visualization was done in MATLAB R2017b software (The MathWorks, Natick, MA, USA). We can define the numerical equilibrium state of the model when the maximum norm of the net force becomes less than a given tolerance, i.e., $\|\mathbf{F}^n\|_\infty = \max_{ij} |\mathbf{F}_{ij}^n| < tol$. In this paper, we run most simulations until a fixed time in order to compare the numerical results with different parameter settings.

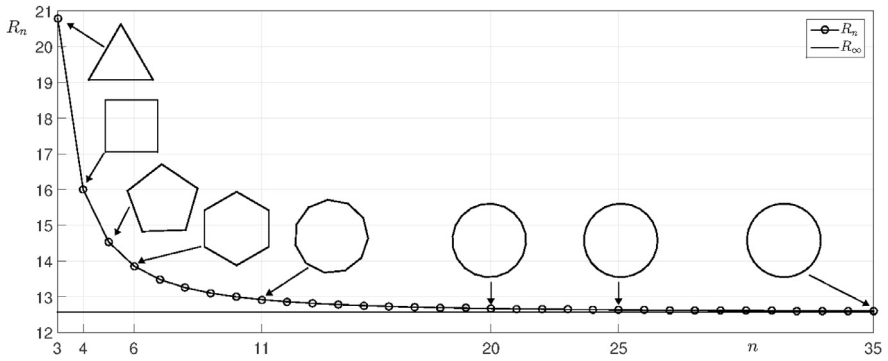

Fig. 8. $R_n = 4n\tan\frac{\pi}{n}$ for $n = 3, 4, \ldots, 35$ (circled line) and $R_\infty = 4\pi$ (solid line).

3.1. Basic mechanism of our model

First, we present the basic mechanism of the proposed model. Let us consider the temporal evolution of the seven initial cells as shown in Fig. 5. Especially, the initial circle in the center deforms to the hexagonal shape by the net force from the neighboring cells as time goes on. In this test, we use the following parameters: $h = 0.125$, $N_x = N_y = 150$, $N_k = 7$, $M = 320$, $\Delta t = 0.05h^2$, $\sigma = 0.1$, and $\alpha = 1$ on $\Omega = (0, 18.76)^2$.

3.2. Various Dirac delta functions

In this section, we investigate the effect of various Dirac delta functions on the cell deformation dynamics. We consider the following three types of delta functions:

- 2-point delta function [24–27]:

$$\phi_1(r) = \begin{cases} 1 - |r| & \text{if } |r| \le 1 \\ 0 & \text{otherwise.} \end{cases}$$

- 4-point delta function [19,25–28]:

$$\phi_2(r) = \begin{cases} (3 - 2|r| + \sqrt{1 + 4|r| - 4r^2})/8 & \text{if } |r| < 1, \\ (5 - 2|r| + \sqrt{9 - 4|r| + 4(2 - |r|)^2})/8 & \text{if } 1 \le |r| \le 2, \\ 0 & \text{otherwise.} \end{cases}$$

- 6-point delta function [25,27–30]:

$$\phi_3(r) = \begin{cases} \frac{61}{112} - \frac{11}{42}|r| - \frac{11}{56}|r|^2 + \frac{1}{12}|r|^3 \\ +\frac{\sqrt{3}}{336}\big(243 + 1584|r| - 748|r|^2 - 1560|r|^3 \\ \quad +500|r|^4 + 336|r|^5 - 112|r|^6\big)^{1/2} & \text{if } 0 \le |r| \le 1, \\ \frac{21}{16} + \frac{7}{12}|r| - \frac{7}{8}|r|^2 + \frac{1}{6}|r|^3 - \frac{3}{2}\phi_3(|r| - 1) & \text{if } 1 \le |r| \le 2, \\ \frac{9}{8} - \frac{23}{12}|r| + \frac{3}{4}|r|^2 - \frac{1}{12}|r|^3 + \frac{1}{2}\phi_3(|r| - 2) & \text{if } 2 \le |r| \le 3, \\ 0 & \text{otherwise} \end{cases}$$

Fig. 6 shows the three different types of Dirac delta functions.

For the numerical test, we use $h = 0.125$, $N_x = N_y = 400$, $N_k = 50$, $M = 320$, $\Delta t = 0.05h^2$, $\sigma = 0.1$, and $\alpha = 1$ on $\Omega = (0, 50)^2$. As shown in Fig. 7, we obtain almost the same results after long time evolution. In this study, we use $\phi_2(r)$ for all numerical tests.

3.3. Ratio of the square of the perimeter to the area of a polygon

We consider a regular polygon, which is equiangular and equilateral. Let n be the total number of the sides of the regular polygon. Let s be the length of a regular polygon. The area of the regular polygon is therefore $A = 0.25ns^2/\tan(\pi/n)$ and perimeter is $P = ns$. To characterize the shape of the regular polygon, we consider the ratio R_n of the square of the perimeter to the area of the polygon as follows.

$$R_n = \frac{P^2}{A} = 4n\tan\frac{\pi}{n}. \tag{4}$$

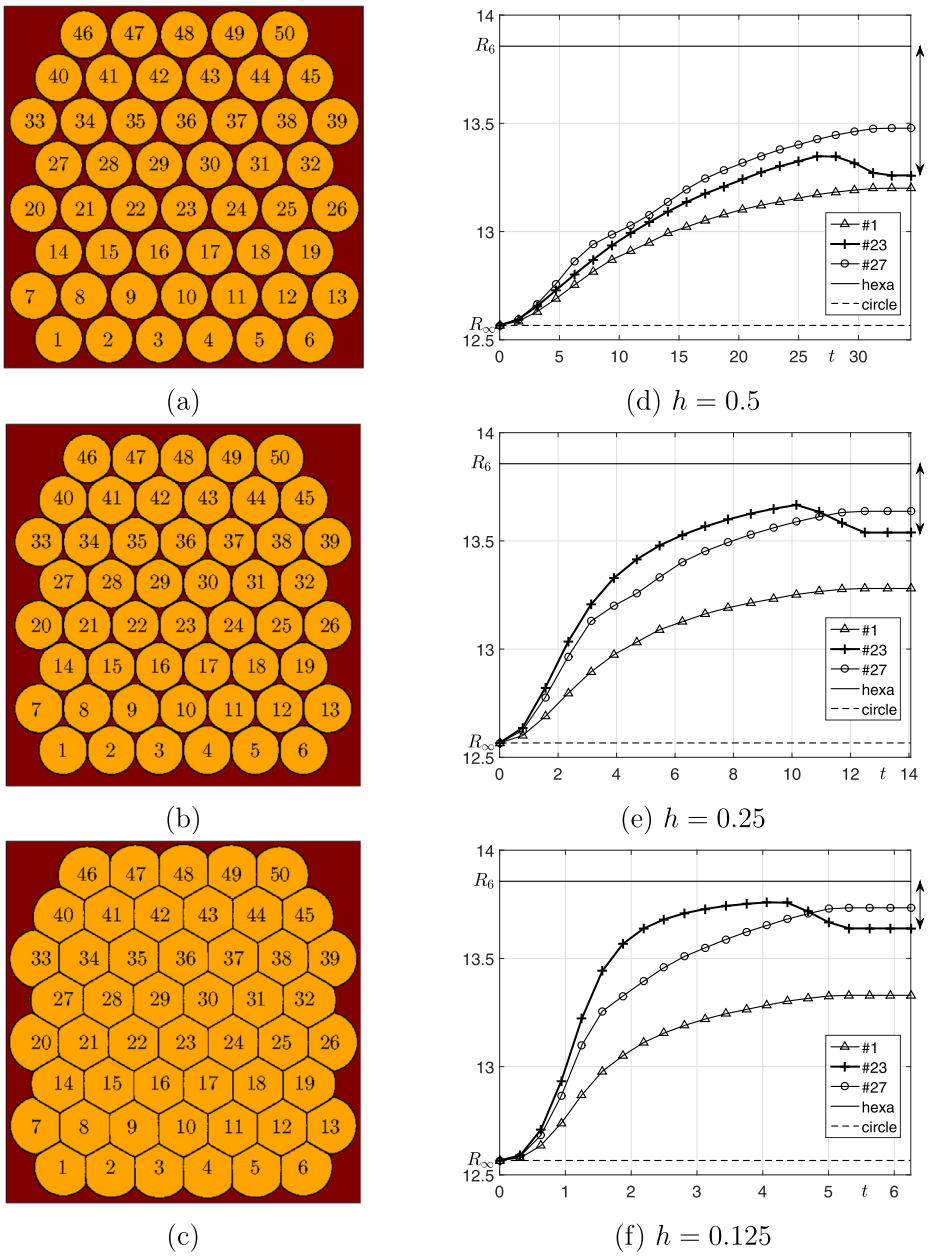

Fig. 9. (a)–(c): Snapshots of the cells with $h = 0.125$ at $t = 0,\ 0.5469$, and 6, respectively. (d)–(f): Temporal evolutions of the ratio R with $h = 0.5,\ 0.25$, and 0.125, respectively.

We note that R_n converges to $R_\infty = 4\pi$ as $n \to \infty$, which is the case of a circle. Fig. 8 shows R_n for $n = 3, 4, \ldots, 35$ and R_∞. In particular, the regular hexagon has $R_6 = 8\sqrt{3} \approx 13.8564$.

3.4. Numerical convergence with respect to h

In this section, we investigate numerical convergence with respect to spatial step size h. For this, we assume the initial condition to be composed of 50 circles with radius $r = 2.225$ on the computational domain $\Omega = (0, 50)^2$, see Fig. 9(a). In numerical tests, the parameters used are $\sigma = 0.1$, $\alpha = 1$, $N_k = 50$, $M = 320$, and $\Delta t = 7.8125\text{e}{-4}$.

When we use $h = 0.125$, we obtain temporal numerical results at $t = 0,\ 0.5469$, and 6 as shown in Fig. 9(a)–(c). As time evolves, initial circles grow and then deform into hexagons.

Now, we calculate the ratio $R = P^2/A$, where P and A denote length and area of each cell, respectively. In this test, we only investigate the ratio of 1st, 23th, and 27th cells. Fig. 9(d)–(f) show the temporal ratio R of 1st, 23th, and 27th cells with

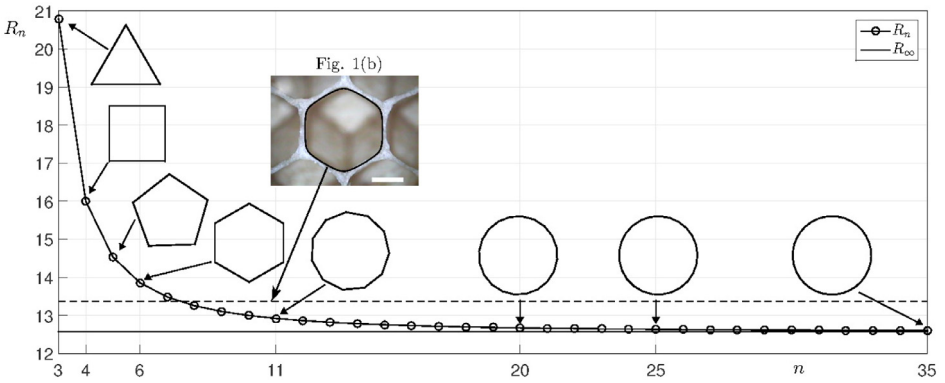

Fig. 10. Ratio of the experiment data (dashed line) which is between a septangle and an octagon.

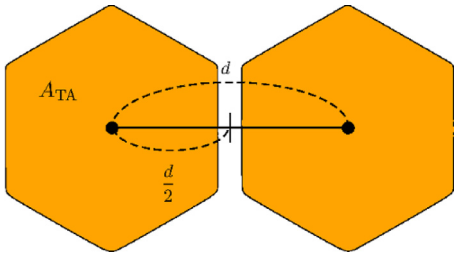

Fig. 11. Schematic of two adjacent cells having distance d between the centers.

respect to $h = 0.5,\ 0.25$, and 0.125, respectively. Regardless of h, each ratio goes to R_6, i.e., the ratio of a regular hexagon. In addition, the gap between the ratio of the 23th cell and regular hexagon decreases as h decreases.

3.5. Effect of a target area A_{TA}

In Fig. 1(b), we can see the rounded hexagonal shape of an Italian honeybee comb cell. This has the ratio 13.3705, which is between a septangle and an octagon, as shown in Fig. 10. This means the equilibrium shape of honeybee comb cell is not a regular hexagon; rather, it is a rounded hexagon. We introduce a target area A_{TA} to control honeycomb cell growth as follows:

$$A_{\mathrm{TA}} = \chi A,$$

where χ is a positive constant and $A = \pi\,(d/2)^2$ is the area of a disk of radius d, which is a distance between the centers of two adjacent cells as shown in Fig. 11.

Next, we perform several numerical simulations to study the effect of A_{TA} with the same initial condition in Fig. 9(a). We use $\alpha = 1, \sigma = 0.1,\ N_k = 50,\ M = 320,\ \Delta t = 7.8125\mathrm{e}{-4}$, and $h = 0.125$. Fig. 12(a)–(d) represent the temporal morphologies of seven cells at $t = 6$ with $\chi = 0.9,\ 0.99,\ 1.08$, and 1.17, respectively. In addition, we can see the temporal evolution of ratio with respect to χ until $t = 6$. As χ increases, the morphologies of the cell converge to the regular hexagonal shape. Especially, the temporal evolution of the ratio with $\chi = 1.08$ agrees well with the experimental data (Fig. 1(b)) as shown in Fig. 12(e).

3.6. Random visit of bees

In this section, we consider the effect of the random visit percentage of bees. The initial configuration is shown at the upper left corner in Fig. 14. The other parameter is the same as in the previous test with $\chi = 1.08$. To assume the random visits of bees, we randomly select a cell and then apply an external force only to it. Fig. 13 illustrates that bees randomly visit the cells for each iteration with 5 out of $N_k = 50$.

Fig. 14 represents the temporal evolution of morphology with 10%, 30%, 50%, 70%, and 100% random visits. Here, the x- and y-axis represent the iteration and cell number (k), respectively.

From the results in the last column, we can confirm that all cases generate similar hexagonal patterns.

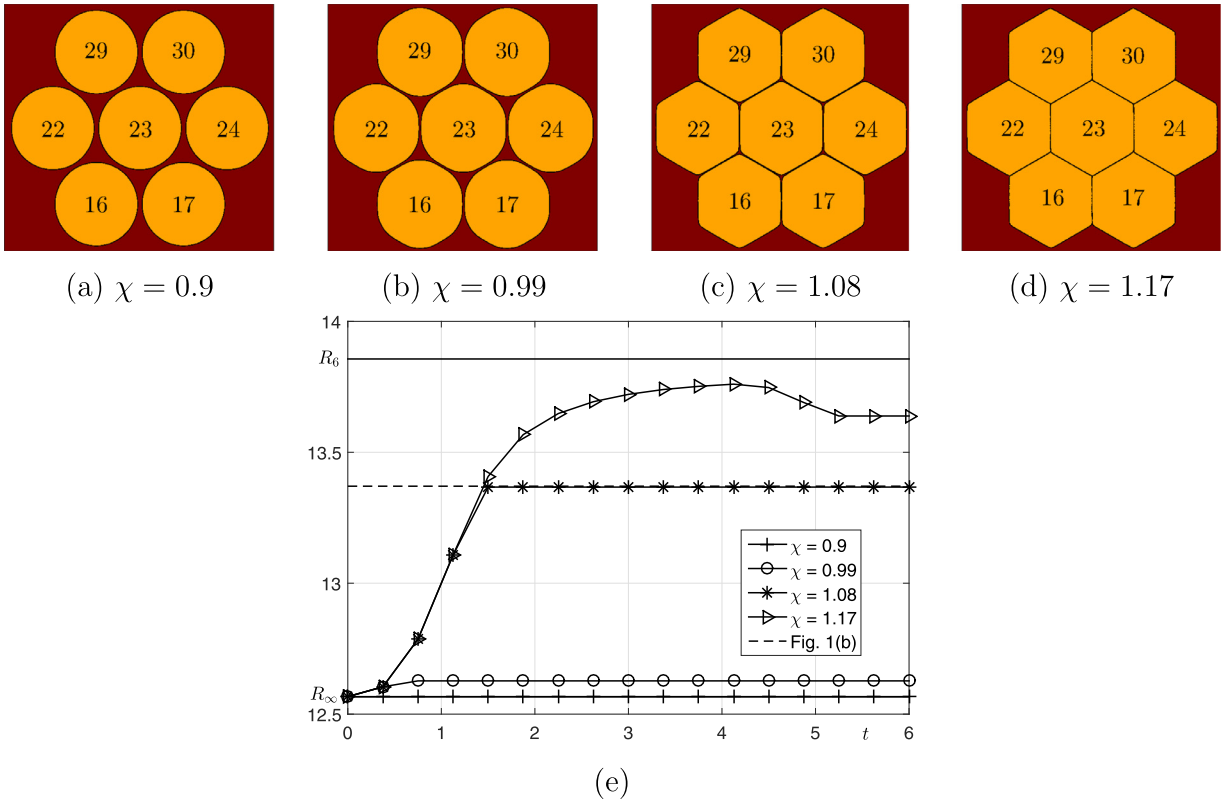

Fig. 12. (a)–(d): Snapshots at time $t = 6$ with different χ values. (e): Temporal evolution of ratio up to time $t = 6$.

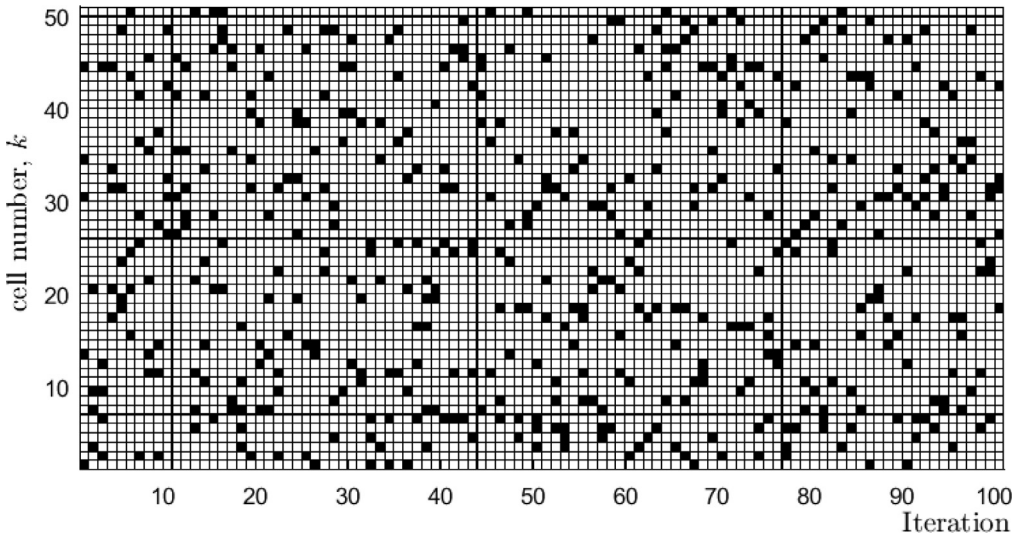

Fig. 13. 10% random visits of bees.

3.7. Comparison with experimental data

To confirm the validity of the proposed model and the numerical method, we compare the numerical results with the experimental data. We consider a basic unit of the hexagonal periodic structure.

Fig. 15 shows the numerical results of the proposed model. In the figure, experimental data are Italian honeybee (Aplis mellifera Liqustica) comb cell at (a) 'birth', and at (c) 2-days old. The new honeycomb cell starts its life as a circular shape however quickly takes on the rounded hexagonal morphology [6]. In this simulation, we use the following parameters:

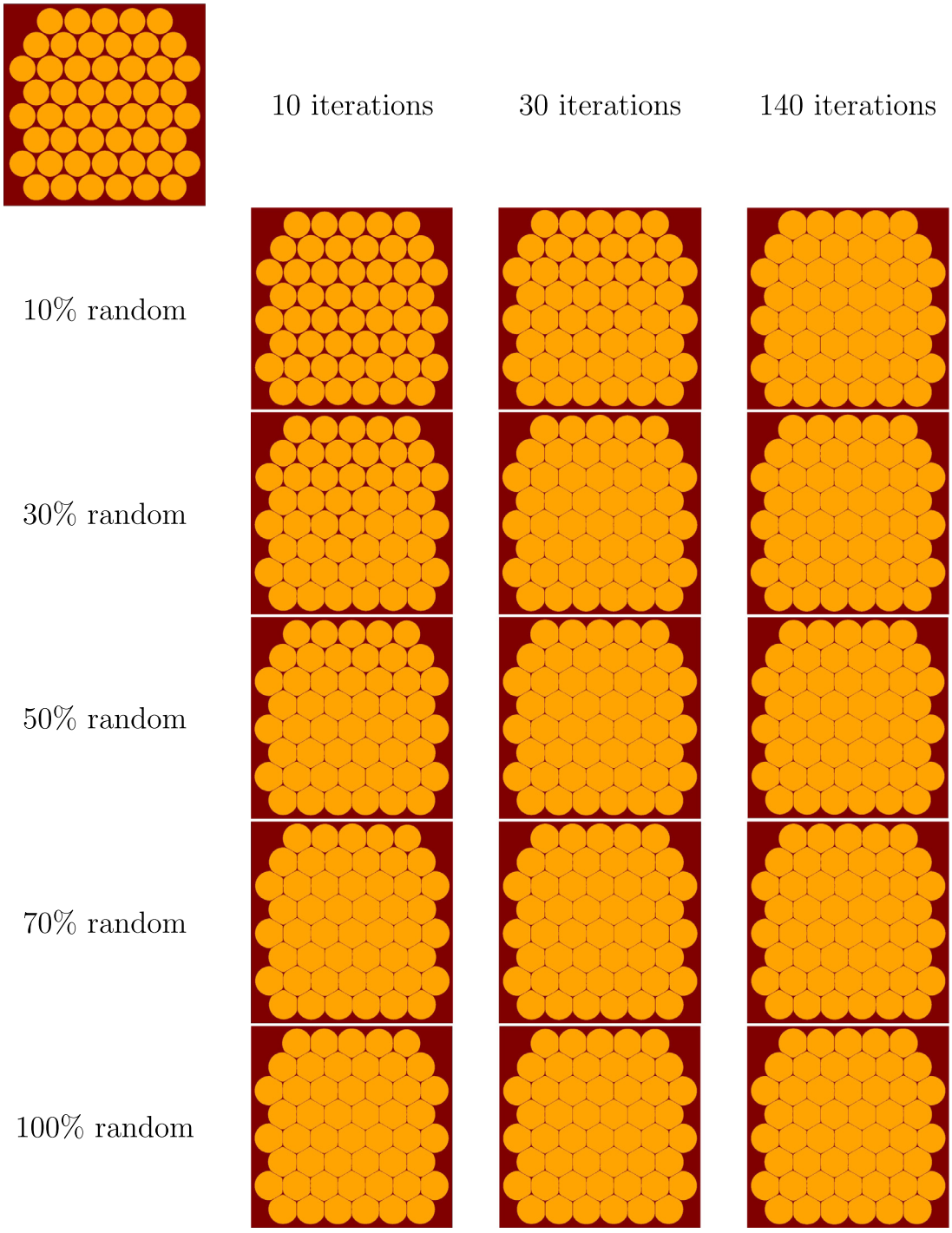

Fig. 14. Temporal evolutions with different percent of random visits.

$\alpha = 1$, $\sigma = 0.1$, $N_x = 14$, $N_y = 24$, $N_k = 2$, $M = 160$, $L_x = 5$, $h = L_x/N_x$, $L_y = N_y h$, and $\Delta t = 0.1h^2$. The initial configuration is composed of circles with a radius $r = 2.225$ as shown in Fig. 15(a). We apply periodic boundary conditions. Fig. 15(b) shows temporal evolution of the boundaries and Fig. 15(c) is the actual experimental data with the numerical solution overlaid. We obtain good agreement between the numerical solution of the mathematical model and the actual pattern development process observed in honeybee combs. The main result is that we can generate hexagonal pattern formation in the honeybee comb using a simple mathematical model, in which the deriving force is the net force coming from the forces exerted outward by the cell boundaries.

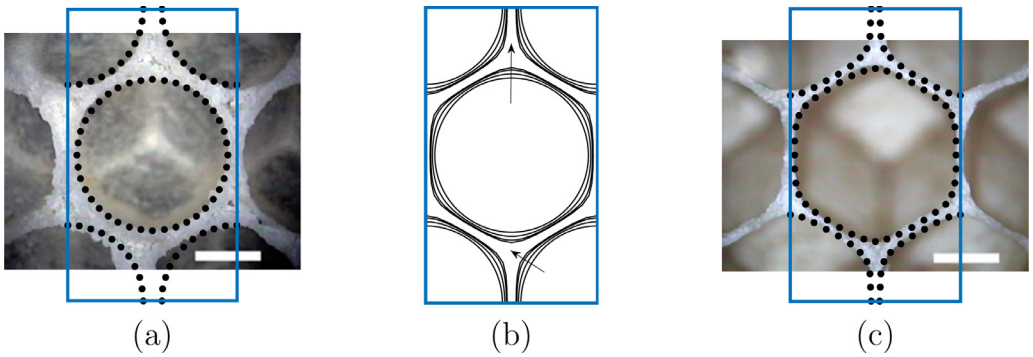

Fig. 15. Overlapped images of scaled simulation result and experimental data. (a) Initial configuration. (b) Temporal evolution of the boundaries. Arrows indicate the evolution direction. (c) Real experimental data with the numerical solution overlaid. Reprinted from Karihaloo et al. [6] with permission from the Royal Society.

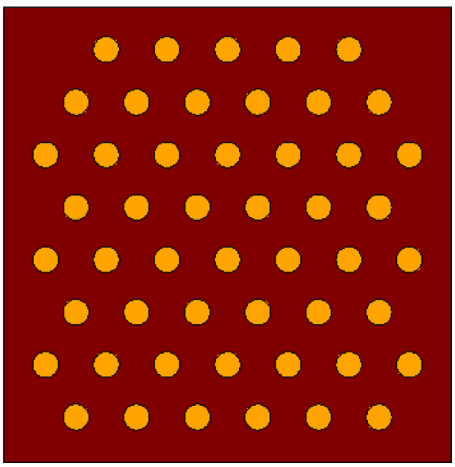

Fig. 16. Initial condition with $r = 1$.

3.8. Stability test

Because we use the explicit Euler's method for the temporal discretization, we have the Courant–Friedrichs–Levy (CFL) condition, $\Delta t\alpha\sigma < 0.5h$. The condition implies the interfaces cannot cross more than one half grid cell in one time step so that they cannot touch each other. We present a stability test to confirm this time step restriction. We use the same parameter values as in Fig. 9 except r and Δt: $\sigma = 0.1$, $\alpha = 1$, $N_k = 50$, and $M = 320$. Initial condition is composed of 50 circles with radius $r = 1$ as shown in Fig. 16.

Fig. 17 shows that the numerical result is stable if the time step satisfies the CFL condition, i.e., $\Delta t\sigma\alpha/h = 0.4$. However, if the condition is not satisfied ($\Delta t\sigma\alpha/h = 0.6$), then the numerical solution is not stable as shown in the second row in Fig. 17.

3.9. Linear computational cost

To show the linear computational cost, we vary the number of cells N_k from 12 to 684. For the numerical simulation, we use the following parameters: $h = 0.125$, $M = 320$, $\Delta t = 0.05h^2$, $T = 500\Delta t$, $\sigma = 0.1$, and $\alpha = 1$. The computational domain used is proportional to the number of N_k.

Fig. 18 shows the effect of the number of cells on the computational cost. The computational cost increases linearly as the number of cells increases.

3.10. Application of the proposed model

The honeycomb shape is applicable in various fields. Honeycomb structures are known for outperforming other cellular materials in terms of both strength and stiffness under shear or compression, see [11] and references therein. A patient-

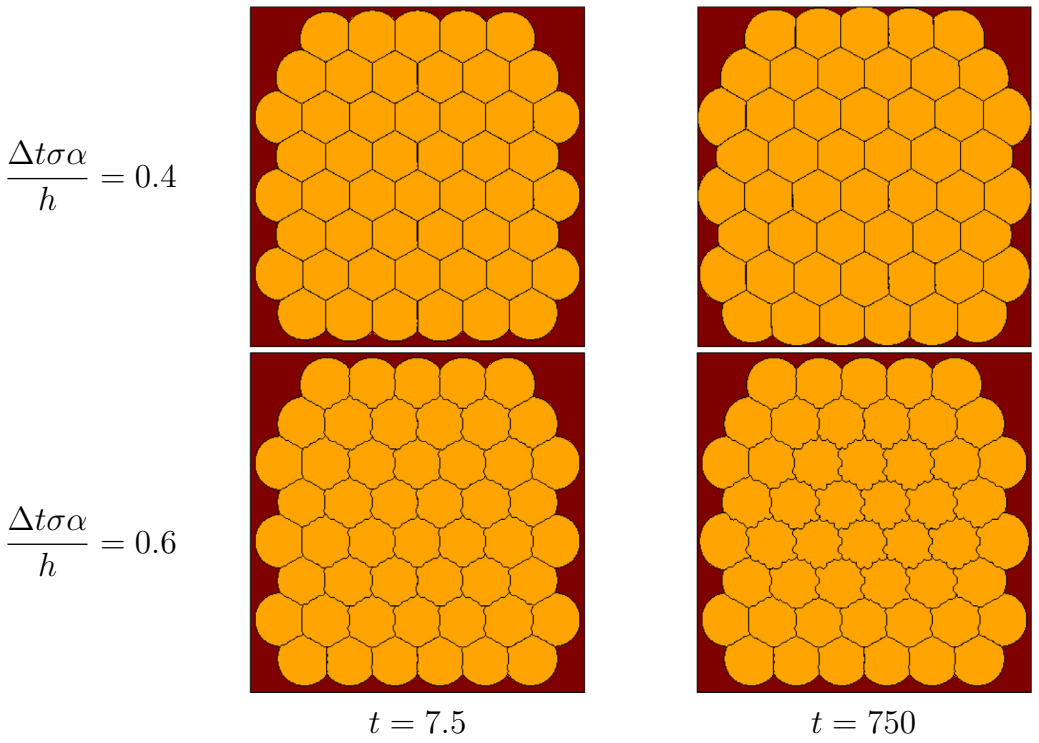

Fig. 17. Comparison of stability results with two different $\Delta t\sigma\alpha/h$ values at times $t = 7.5$ and $t = 750$.

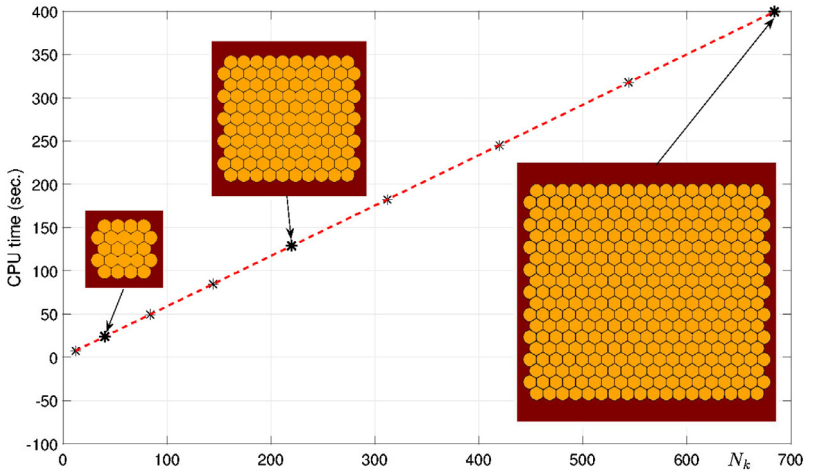

Fig. 18. Graph of CPU time versus the total number of cells N_k.

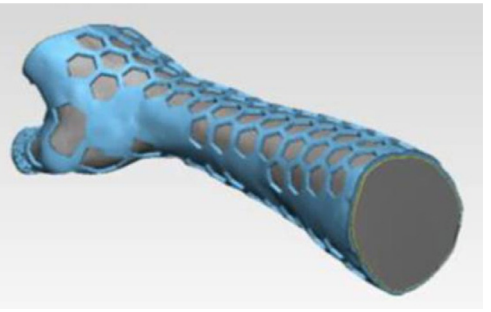

Fig. 19. A patient-specific 3D-printed cast. Reprinted from Fitzpatrick et al. [31] with permission from Knowledge E.

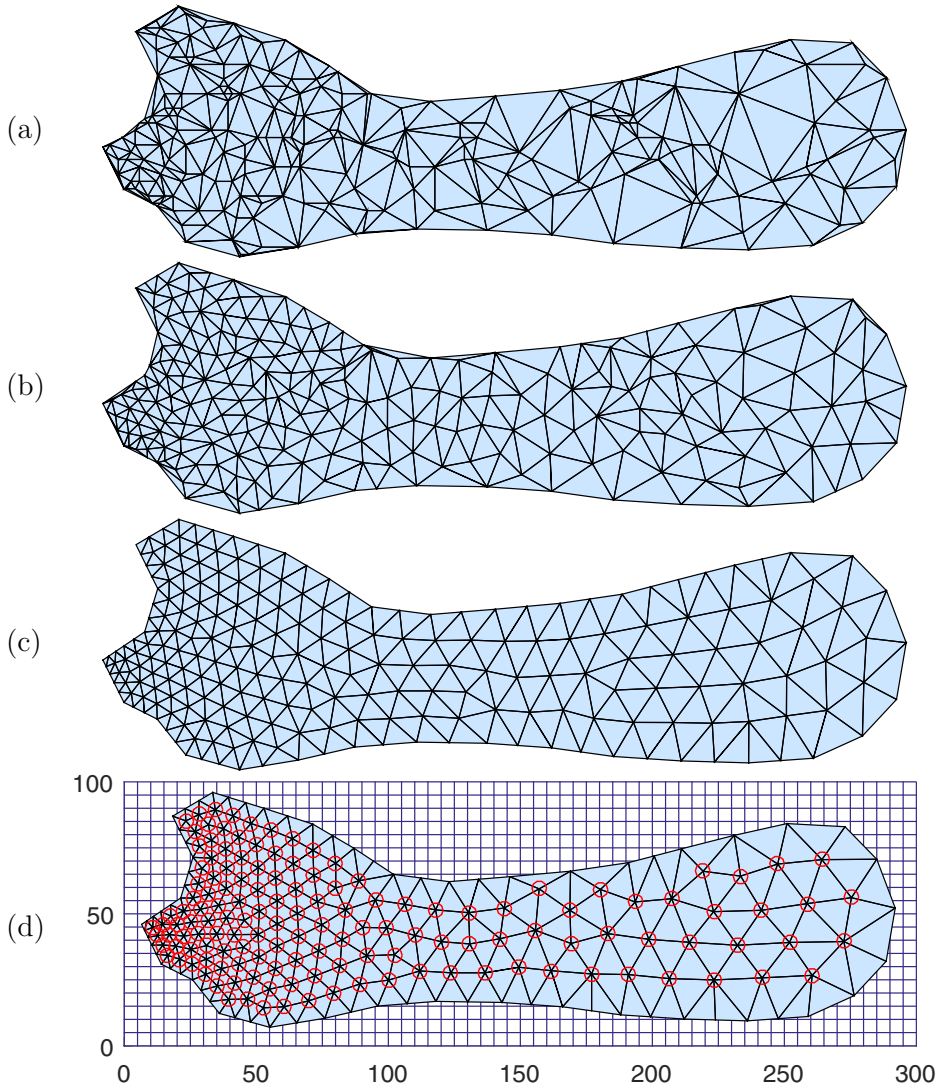

Fig. 20. Generation of an initial condition using the DistMesh algorithm [32].

specific 3D-printed cast is an example in the medical field as shown in Fig. 19. The honeycomb shape allows for access to the skin if there is irritation, and allows airflow to ensure there is no chance for the skin to become infected [31].

As an application of the proposed method, we consider a hexagonal type pattern formation in an arbitrary polygonal domain. Fig. 20 shows generation of an initial condition using the DistMesh algorithm [32], which is an open source MATLAB mesh generator for creating a triangular mesh with nonuniform mesh densities.

In Fig. 21, we use simulation parameters $\alpha = 1,\ \sigma = 0.1,\ h = 0.5,\ \Delta t = 0.1h^2,\ N_k = 145,\ M = 160,$ and 600×200 mesh grid on the computational domain $\Omega = (0, 300) \times (0, 100)$. The initial condition for the cast design is defined by using the points obtained through the DistMesh algorithm as shown in Fig. 20(d) and the sizes of radii are adjusted according to the value of x; $r(x) = 0.00004x^2$. To design the cast, we perform a post-process to shrink each cell boundary by 20%, see Fig. 21.

Note that we can generate regular hexagonal pattern using a phase-field crystal equation:

$$\frac{\partial \varphi}{\partial t} = M\Delta(\varphi^3 + (1-\epsilon)\varphi + 2\Delta\varphi + \Delta^2\varphi), \tag{5}$$

where M is a mobility and ϵ is a constant. In the phase-field crystal model, the number density of atoms approximates with a continuous phase field φ which is called crystal, see references [33,34] for more details about the phase-field crystal equation and its numerical simulations. Also, we can obtain a regular hexagonal pattern by Turing instability, see [35,36] for various Turing systems.

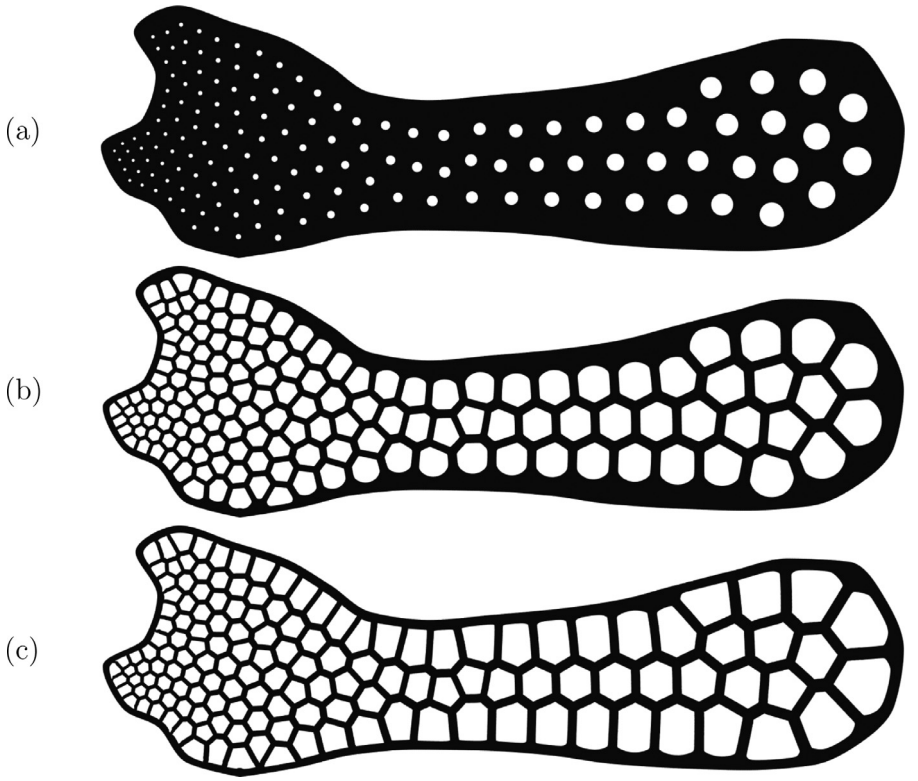

Fig. 21. Generation of a cast design using the proposed algorithm. Snapshots of numerical solution at (a) $t = 0$, (b) $t = 125$, and (c) $t = 250$.

4. Conclusions

In this work, we proposed a mathematical model using the immersed boundary method, for the transformation of circular cells in a honeycomb to hexagonal cells. Although the model is simple, it captures the main transformation mechanism. This work can be extended to model and simulate a fully three-dimensional honeycomb structure formation. In future work, we will develop a three-dimensional model and a numerical method for the three-dimensional case.

Acknowledgements

The authors thank the reviewers for the constructive and helpful comments on the revision of this article. The first author (D. Jeong) was supported by the National Research Foundation of Korea (NRF) grant funded by the Korea government (MSIP) (NRF-2017R1E1A1A03070953). The corresponding author (J.S. Kim) was supported by Basic Science Research Program through the National Research Foundation of Korea (NRF) funded by the Ministry of Education (NRF-2016R1D1A1B03933243).

Appendix

Geometric derivation of the normal vector

We present a geometric derivation without using the quadratic polynomial approximation. The unit normal vector ($\mathbf{n}_l$) at the point (x_l, y_l) can be defined by interpolation using the relation between two nearby points.

Fig. 22 represents the schematic of normal vector $\mathbf{m}_l$ at (x_l, y_l). The distance Δs_l is defined as $\Delta s_l = \sqrt{(x_l - x_{l-1})^2 + (y_l - y_{l-1})^2}$. A normal vector to the line segment connecting the points (x_l, y_l) and (x_{l-1}, y_{l-1}) is

$$\left(\frac{y_l - y_{l-1}}{\Delta s_l}, \frac{x_{l-1} - x_l}{\Delta s_l}\right)$$

and similarly, the normal vector for the points (x_{l+1}, y_{l+1}) and (x_l, y_l) is

$$\left(\frac{y_{l+1} - y_l}{\Delta s_{l+1}}, \frac{x_l - x_{l+1}}{\Delta s_{l+1}}\right).$$

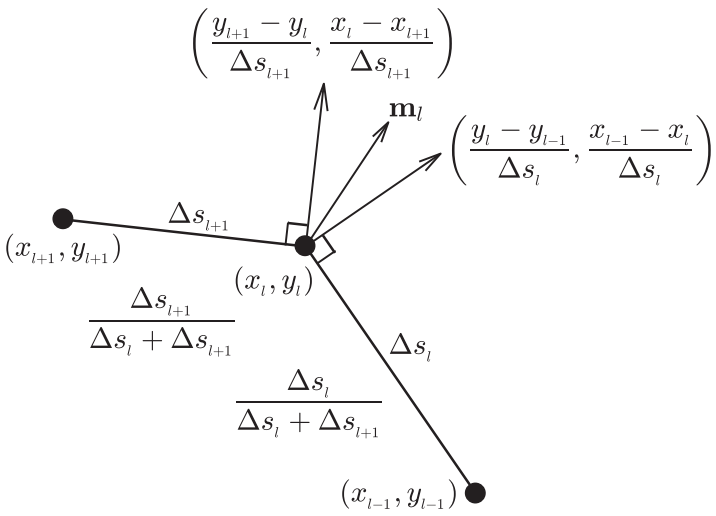

Fig. 22. Schematic of normal vector $\mathbf{m}_l$ at point (x_l, y_l).

Therefore, we obtain the normal vector $\mathbf{m}_l$ by a linear interpolation,

$$\mathbf{m}_l = \frac{\Delta s_{l+1}}{\Delta s_l + \Delta s_{l+1}}\left(\frac{y_l - y_{l-1}}{\Delta s_l}, \frac{x_{l-1} - x_l}{\Delta s_l}\right) + \frac{\Delta s_l}{\Delta s_l + \Delta s_{l+1}}\left(\frac{y_{l+1} - y_l}{\Delta s_{l+1}}, \frac{x_l - x_{l+1}}{\Delta s_{l+1}}\right).$$

Finally, we have the unit normal vector, $\mathbf{n}_l = \mathbf{m}_l / |\mathbf{m}_l|$.

References

[1] Bauer D, Bienefeld K. Hexagonal comb cells of honeybees are not produced via a liquid equilibrium process. Naturwissenschaften 2013;100(1):45–9.
[2] Zhang L, Zhang F, Ruan S. Linear and weakly nonlinear stability analyses of turing patterns for diffusive predator? Prey systems in freshwater marsh landscapes. Bull Math Bio 2017;79(3):560–93.
[3] Karst NJ, Geddes JB, Carr RT. Model microvascular networks can have many equilibria. Bull Math Bio 2017;79(3):662–81.
[4] Koltover I, Salditt T, Radler JO, Safinya CR. An inverted hexagonal phase of cationic liposome-DNA complexes related to DNA release and delivery. Science 1998;281(5373):78–81.
[5] Bergman DJ, Ishay JS. Do bees and hornets use acoustic resonance in order to monitor and coordinate comb construction? Bull Math Bio 2007;69(5):1777–90.
[6] Karihaloo BL, Zhang K, Wang J. Honeybee combs: how the circular cells transform into rounded hexagons. J R Soc Int 2013;10(86):20130299.
[7] Pirk CWW, Hepburn HR, Radloff SE, Tautz J. Honeybee combs: construction through a liquid equilibrium process? Naturwissenschaften 2004;91(7):350–3.
[8] Davis JM, Pozrikidis C. Self-sustained oscillations in blood flow through a honeycomb capillary network. Bull Math Biol 2014;76(9):2217–37.
[9] Peskin CS. Numerical analysis of blood flow in the heart. J Comput Phys 1977;25(3):220–52.
[10] Wang Y, Liu Z, Huang Y, Han B, Yang G. Micropatterned polymer surfaces induced by nonsolvent. Langmuir 2006;22(4):1928–31.
[11] Zhang Q, et al. Bioinspired engineering of honeycomb structure-using nature to inspire human innovation. Prog Mater Sci 2015;74:332–400.
[12] Chawla A, Mukherjee S, Kumar D, Nakatani T, Ueno M. Prediction of crushing behaviour of honeycomb structures. Int J Crashworthiness 2003;8(3):229–35.
[13] Yamashita M, Gotoh M. Impact behavior of honeycomb structures with various cell specifications numerical simulation and experiment. Int J Impact Eng 2005;32(1):618–30.
[14] Miller W, Smith CW, Evans KE. Honeycomb cores with enhanced buckling strength. Compos Struct 2011;93(3):1072–7.
[15] Papka SD, Kyriakides S. In-plane compressive response and crushing of honeycomb. J Mech Phys Solids 1994;42(10):1499–532.
[16] Lee W, Jung E. A multiscale model of cardiovascular system including an immersed whole heart in the cases of normal and ventricular septal defect (VSD). Bull Math Bio 2015;77(7):1349–76.
[17] Lee S, Jeong D, Lee W, Kim J. An immersed boundary method for a contractile elastic ring in a three-dimensional newtonian fluid. J Sci Comput 2016;67(3):909–25.
[18] Peskin CS, Printz BF. Improved volume conservation in the computation of flows with immersed elastic boundaries. J Comput Phys 1993;105(1):33–46.
[19] Peskin CS. The immersed boundary method. Acta Numer 2002;11:479–517.
[20] Terzopoulos D, Platt J, Barr A, Fleischer K. Elastically deformable models. Comput Graph (ACM) 1987;21(4):205–14.
[21] Ricciardi TR, Wolf WR, Bimbato AM. Fast multipole method applied to lagrangian simulations of vortical flows. Commun Nonlinear Sci Numer Simul 2017;51:180–97.
[22] Durante D, Rossi E, Colagrossi A, Graziani G. Numerical simulations of the transition from laminar to chaotic behaviour of the planar vortex flow past a circular cylinder. Commun Nonlinear Sci Numer Simul 2017;48:18–38.
[23] Udaykumar HS, Kan HC, Shyy W, Tran-Son-Tay R. Multiphase dynamics in arbitrary geometries on fixed cartesian grids. J Comput Phys 1997;137(2):366–405.
[24] Leveque RJ, Li Z. The immersed interface method for elliptic equations with discontinuous coefficients and singular sources. SIAM J Numer Anal 1994;31:1019–44.
[25] Shin SJ, Huang WX, Sung HJ. Assessment of regularized delta functions and feedback forcing schemes for an immersed boundary method. Int J Numer Methods Fluids 2008;58:263–86.
[26] Yang X, Zhang X, Li Z, He GW. A smoothing technique for discrete delta functions with application to immersed boundary method in moving boundary simulations. J Comput Phys 2009;228:7821–36.
[27] Lee HG, Kim J. Regularized dirac delta functions for phase field models. Int J Numer Methods Eng 2012;91(3):269–88.

[28] Griffith BE, Peskin CS. On the order of accuracy of the immersed boundary method: higher order convergence rates for sufficiently smooth problems. J Comput Phys 2005;208:75–105.
[29] Griffith BE, Hornung RD, McQueen DM, Peskin CS. An adaptive, formally second order accurate version of the immersed boundary method. J Comput Phys 2007;223:10–49.
[30] Stockie JM. Analysis and computation of immersed boundaries, with application to pulp fibres. University of British Columbia; 1997. Doctoral dissertaion.
[31] Fitzpatrick AP, Mohanned MI, Collins PK, Gibson I. Design of a patient specific. 3D Printed Arm Cast KnE Eng 2017;2(2):135–42.
[32] Persson PO, Strang G. A simple mesh generator in MATLAB. SIAM Rev 2004;46(2):329–45.
[33] Dehghan M, Mohammadi V. The numerical simulation of the phase field crystal (PFC) and modified phase field crystal (MPFC) models via global and local meshless methods. Comput Methods Appl Mech Eng 2016;298:453–84.
[34] Dehghan M, Abbaszadeh M. The meshless local collocation method for solving multi-dimensional Cahn–Hilliard. Swift–Hohenberg and phase field crystal equations 2017;78:49–64.
[35] Dehghan M, Abbaszadeh M. Numerical study of three-dimensional turing patterns using a meshless method based on moving kriging element free Galerkin (EFG) approach. Comput Math Appl 2016;72(3):427–54.
[36] Lacitignola D, Bozzini B, Frittelli M, Sgura I. Turing pattern formation on the sphere for a morphochemical reaction-diffusion model for electrodeposition. Commun Nonlinear Sci Numer Simul 2017;48:484–508.